Materials Research. 2022; 25:e20220242
DOI: https://doi.org/10.1590/1980-5373-MR-2022-0242

Study on the Strengthening Mechanism of Rare-Earth Element Ce on the Laser Welded Joints of Magnesium Alloys

***Chen Yanfei*[a], *Zhu Zhengqiang*[a*], *Zhao Fei*[a], *Zhou Jixue*[b]**

[a]*Nanchang University, Advanced Manufacturing School, Nanchang 330031, PR China.*
[b]*Shandong Academy of Sciences, Advanced Materials Institute, Jinan 250014, PR China.*

Received: May 16, 2022; Revised: September 16, 2022; Accepted: October 17, 2022

The thermomechanical stability of majority precipitates formed by conventional alloying elements in magnesium alloys is generally poor. Hence the morphology and structure of these precipitates are highly susceptible to the welding thermal cycle, which results in the softening of the heat-affected zone (HAZ). Rare-earth (RE) precipitates are generally thermodynamically stable. Therefore, it is necessary to conduct an in-depth discussion on whether RE precipitates reduce the softening of the HAZ. In this paper, Ce-containing magnesium alloy was successfully welded by fiber laser welding. Scanning electron microscope (SEM), X-ray diffraction (XRD), energy dispersive spectrometer (EDS), and micro-hardness tester were employed to analyze the welded joints. Consequently, the distribution characteristics of RE precipitates in both fusion zone (FZ) and HAZ were revealed. Moreover, based on the solution experiments of the welded joints, the evolution mechanism of the precipitates in welded joints during the thermal cycle was deduced, and the softening mechanism of the HAZ was clarified. Thereafter, the relative intrinsic mechanism of RE precipitates in reducing the softening of the HAZ and improving the mechanical properties of FZ was explored. The results showed that the HAZ was narrow, with a width of only 100-200 μm. The morphology and distribution of the less thermally stable $Mg_{17}Al_{12}$ precipitated in HAZ changed significantly after the thermal cycle. In contrast, RE precipitates remained stable, which is extremely important for reducing the softening of the HAZ. In addition, the precipitates in FZ were transformed into micron-sized particles and precipitated at the edge of dendrites, resulting in a hardness improvement of the FZ.

Keywords: *Laser welding, Rare-earth magnesium alloy, Cerium, Heat-affected zone, Softening.*

1. Introduction

Lightweight is one of the most critical development directions in transportation and aviation industries nowadays[1]. Magnesium alloys, the lightest structural metallic material, are increasingly used to replace some traditional materials in auto parts due to their high specific strength/specific stiffness, recyclability, abundant resources, and excellent processing properties[2]. However, the heat resistance of magnesium alloys is poor, and the morphology and distribution of the strengthening phases formed by most conventional elements in the alloys are highly susceptible to thermal cycling[3], which limits the application of magnesium alloys. For example, the most critical strengthening precipitate in Mg-Al-Zn magnesium alloys (AZ series), $Mg_{17}Al_{12}$, softens at temperatures above 120°C[4,5], and the melting point of $Mg_{17}Al_{12}$ is only 473°C[6,7]. The same is for Mg-Zn-Zr magnesium alloys (ZK series); although they have obtained good comprehensive mechanical properties by refining the grains with the addition of Zr element, the melting points of the major precipitates in the alloys such as MgZn, $MgZn_2$ (laves phase) and Mg_2Zn_3 are just 342°C[8], 808°C[9] and 416°C[8], respectively, indicating the poor heat resistance as well. These less thermally stable precipitates in heat-affected zone easily melt and re-aggregate, forming coarse-sized precipitates at grain boundaries during the brief welding thermal cycle[10], which in turn has a typical splitting effect on the matrix during plastic deformation due to the huge difference in elastic constants with the matrix[11]. Moreover, the original well-designed, finely distributed precipitates are drastically reduced because of the thermal melting or dissolution, thus weakening the initial precipitation strengthening or precipitated-phase strengthening of the matrix[12]. Therefore, the softening of the heat-affected zone of the weld is extremely serious, and how to achieve high-quality welding of magnesium alloys has become the frontier of magnesium alloy research[13].

Highly thermodynamically stable precipitates have a significant role in reducing the softening of welded joints[14,15]. In particular, the thermodynamic stability of precipitates formed by rare-earth elements is generally much higher than that of conventional elements[16]. For example, researchers have explored the synthesis of precipitates with good thermodynamic stability by conventional alloying elements, such as Al_2Ca, Mg_2Si, and Al_4Sr, which are formed by adding Ca, Si, and Sr elements, and their melting points are 1079°C[17,18], 1087°C[19,20], and 1040°C[21-23], respectively. Although the thermodynamic stability of these precipitates is not bad, that of the precipitates composed of rare-earth elements such as Pr, Nd, Gd, Dy, La, Ce, Y, etc., is much higher. For example, the melting

*e-mail: 350906320003@email.ncu.edu.cn

point of $Al_{11}Pr_3$ is up to 1240°C[6], the Al_2Pr has a melting point of 1480°C[6], and the melting points of the other rare-earth precipitates such as $Al_{11}Nd_3$, Al_3Nd, $Al_{11}La_3$, Al_2La, $Al_{11}Ce_3$, Al_4Ce, Al_2Ce, Al_2Y are 1235°C[6], 1680°C[6], 1240°C[24], 1405°C[24,25], 1235°C[6], 1251°C[26], 1480°C[6], 1485°C[6], respectively. However, it is noteworthy that Mg-RE precipitates may also be formed when RE elements are added to the aluminum-free magnesium alloys owing to their electronegativity. The Mg-RE precipitates that have been characterized include $Mg_{41}Nd_5$[27,28], Mg_5Gd[29], $Mg_{24}Dy_5$[30], $Mg_{24}Y_5$[31], MgCe[32], Mg_2Ce[33], Mg_3Ce[34], $Mg_{12}Ce$[35], $Mg_{17}Ce_2$[35], et al., but the results find that their melting points are markedly lower than that of the Al-RE precipitates. The melting points of the above-mentioned Mg-RE precipitates are only 545°C[27,28], 545°C[29], 535°C[30], 566°C[31], 505°C[36], 750°C[37], 796°C[37], 598°C[38], and 617°C[37], respectively. All these examples demonstrate that the key to reducing the softening of the heat-affected zone lies in obtaining highly thermodynamically stable Al-RE precipitates. Hence the precipitates in HAZ remain stable during the thermal cycle, which in turn significantly reduces the width of the heat-affected zone. Whereas the precious rare-earth elements are both expensive and impractical for many commercial applications[2], a comparison finds that the melting points of Al-Ce precipitates are almost at the same level as that of Al-Pr and Al-Nd precipitates, while the cost of rare-earth Ce is much lower than the latter. Therefore, adding high-abundance, low-cost rare-earth elements (such as La, Ce, and Y) and forming thermally stable precipitates with Al elements in the magnesium alloys becomes an ideal way to improve the mechanical properties of welded joints[39].

Laser welding also has a role in reducing the size of the heat-affected zone, mainly due to the high energy density and low heat input of the laser beam, which makes the fusion zone heat up quickly[40]. As a result, the time the base metal is affected by the welding heat input is relatively short. Obviously, the combination of laser welding and rare-earth precipitates may be a potential solution for reducing the softening of the heat-affected zone of magnesium alloy welds[41]. Jun Dai et al.[42] verified this by performing laser welding on a 10mm thick NZ30K rare-earth magnesium alloy. The results found that the precipitation strengthening effect of rod-like and tadpole-shaped rare-earth precipitates in the welded joint contributed 79% of the total yield strength of the alloy[42]. Moreover, the width of the heat-affected zone was only 200-400 μm[43], further reflecting that the combination of laser welding and rare-earth precipitates is one of the most potent methods for improving the performance of magnesium alloy welded joints.

Ce-containing magnesium alloys are less expensive and suitable for commercial applications, especially for welding wire manufacturing and weld joint strengthening. Liming Liu et al.[44] successfully welded (laser-TIG hybrid welds) the dissimilar metals of 6061 aluminum alloy and AZ31 magnesium alloy by adding Ce foils as interlayers. The results indicated that Ce refined the grains on both sides of the joint, and the unique elongated morphology of Ce-containing precipitates reduced the thermal cracks in welded joints. The research by R.P. Dobriyal et al.[45] further found that typical $Al_{11}Ce_3$, Al_2Ce, and $Mg_{17}Al_{12}$ precipitates were uniformly distributed both in the friction stirred zone (FSZ) and the thermo-mechanical affected zone (TMAZ) of the friction stir welded joint of AE42 alloy. The precipitates in FSZ were stirred and broken into pieces with sizes of 5-8 μm, the corresponding hardness test along the width direction of the joint reflected that those smaller-sized, uniformly-dispersed Ce-containing precipitates had a significant effect on improving the hardness and strength of the FSZ. The tensile test performed by YU Sirong et al.[46] highly agreed with that. The ultimate tensile strength (UTS) of the friction stir welded joint of an AZ31B magnesium alloy comprising 0.5wt% Ce was found to be 238MPa, which was only 32MPa lower than that of the base metal (270.41MPa). These examples above illustrate the role of Ce element in improving the microstructure and mechanical properties of welded joints. However, most of these studies are limited in the characterization of properties of the welded joint, and the detailed formation mechanism of precipitates in the weld zone and HAZ is not clearly elucidated. And also, there are few studies on fusion welding of rare-earth magnesium alloys. Hence, more research is needed.

Herein, the Mg-Al-Ce magnesium alloy was set as the research object, and well-formed joints were successfully obtained by fiber laser welding. With the aid of microstructure and composition analysis, the distribution characteristics of rare-earth precipitates in FZ and HAZ of the joint were revealed. Moreover, the evolution mechanism of the precipitates in FZ and HAZ during the thermal cycle was clarified based on solution experiments. Thereafter, the strengthening mechanism of rare-earth precipitates on improving the comprehensive mechanical properties of the welded joint was explored; and the internal principle of rare-earth precipitates on reducing the softening of the HAZ was revealed, which provided a feasible welding solution for magnesium alloys serving in thermal cycling conditions.

2. Sample Preparation and Research Details

2.1. Material details

The experimental material used in this work is a rare-earth magnesium alloy comprising 0.4wt.% Ce. The composition is shown in Table 1. The alloy was smelted from pure magnesium, aluminum, zinc blocks, Mg-Mn master alloy, and Mg-30wt.% Ce master alloy. The melting temperature was set at 750°C, the shielding gas was a mixture of CO_2 and SF_6, the volume fraction of SF_6 in the mix was 0.5%, and the flow rate of the mixed gas was 5L/min. Stirred continuously for 2 minutes after the Mg-Ce master alloy was added for 10 minutes, followed by slagging, resting, and casting in a metal mold preheated to 200°C, obtaining ingots with a

Table 1. The composition of the rare-earth magnesium alloy comprising 0.4wt.% Ce (wt.%).

Element	Al	Zn	Mn	Si	Fe	Cu	Ce	Mg
Contents	3.156	1.098	0.385	0.167	0.029	0.014	0.436	Balance

diameter of 100 mm. Then the ingots were cut into sheets with a size of 50mm×10mm×0.7mm by a linear cutting machine. Thereafter, the grinding (with 1500# abrasive paper), cleaning (with alcohol), and drying procedures were applied to prepare sheets for laser welding.

2.2. Welding process

The laser welding was performed at a laser welding system consisting of a 3KW fiber laser (IPG Photonics YLS-3000-SM) and a robotic arm (KUKA KR 30 R2100). The welding form was a single-sided lap welding; the overlap amount was 15mm. The welding power was set at 500W, the laser head was 10° off the vertical direction, the defocus distance was 0mm, and the welding speed was 5mm/s (300mm/min). During the welding process, the welding sample was properly fixed on the welding table and protected by argon gas until the joint was completely cooled. The ventilation direction of the shielding gas was 60° from the welding direction. The schematic diagram is shown in Fig. 1.

2.3. Test details

Test specimens were cut from the welded joints by a linear cutting machine. Part of the base metal and welded joint samples were solution treated with processes of 440°C×8h and 440°C×20h, respectively. Microstructure observation was conducted with a Nikon LV150NA optical microscope (OM) and ZEISS EVO MA 10 scanning electron microscope (SEM) after inlaying (with epoxy resin), grinding, polishing, and etching. Meanwhile, the grinding and polishing were carried out with a Buehler EcoMet 30 grinder-polishers. 400#, 800#, and 1500# silicon carbide grinding papers were successively used for grinding. While polishing cloth and 1μm diamond suspension were used for polishing. The etching time was 5s, and the etchant used was prepared with 99ml deionized water, 1ml nitric acid, and 1g oxalic acid. Composition analysis was performed with the aid of Oxford X-Max energy dispersive spectrometer (EDS) and Panalytical XPert Powder X-ray diffractometer (XRD), the scan speed of XRD was 2°/min. For the hardness test, a Huaying HV-1000 type micro-hardness tester was used, the test force was 0.5Kgf (4.903N), and the holding time was 10s. The indentations in the fusion zone were centered on the contact interface of the two sheets, and the horizontal and vertical spacing were both 150μm. While for the solution-treated welded joint, the hardness was measured along the bonded interface (bonding line) of the fusion zone and base metal, as well as on the right and left sides, which were 150μm away from the bonding line, and the test paths were parallel to the bonding line. The test details are elaborated in Fig. 2.

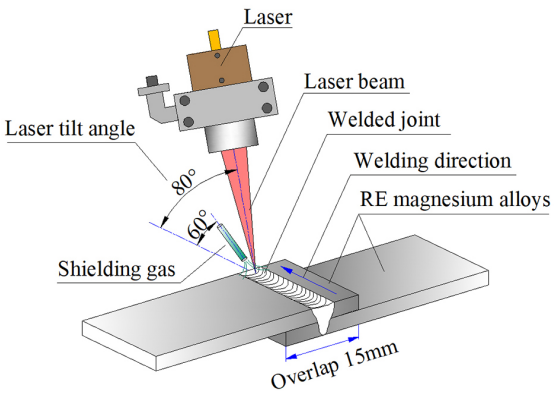

Figure 1. The schematic diagram of laser welding.

3. Experimental Results

3.1. Microstructure and composition of the base metal

The microstructure of the base metal (BM) and the morphology of the precipitates in BM are shown in Fig. 3. As can be seen from the figures, the grains of the base metal are equiaxed, with a size of 300-400 μm. Precipitates are mainly distributed at the grain boundaries in discontinuous granular or large-sized island shapes. Also, a small fraction of granular, rod-like or needle-like precipitates is precipitated in the grains. The back-scattered electron (BSE) image in Fig. 3(c) demonstrates a distinct contrast difference between the island-shaped precipitates at grain boundaries and the granular or needle-like precipitates in grains, in which the precipitates at grain boundaries are in gray, while the

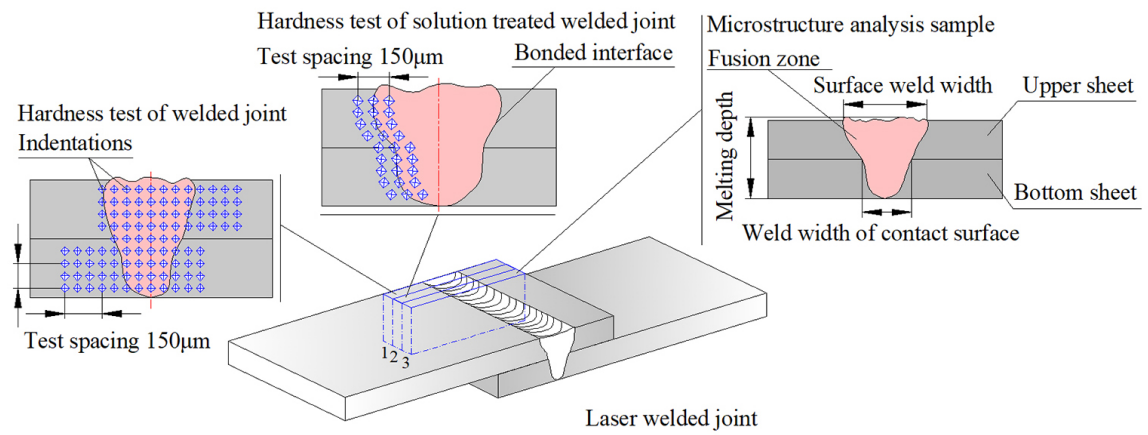

Figure 2. The schematic diagram of test samples.

precipitates in grains are in bright white. Since the contrast in BSE image is related to the atomic number, it is concluded that the elemental composition of the above-mentioned precipitates is different. Hence, EDS is needed for the compositional analysis.

EDS mapping was used to further analyze the elemental composition of precipitates in base metal. The results are shown in Fig. 4. Obviously, precipitates in granular or short rod morphology are mainly composed of Al, Mn, and Ce elements; while the long needle-like precipitates are composed of Al and Ce elements, as outlined in Fig. 4(c,e,f). With the aid of EDS point analysis, the atomic ratio of elements in precipitates is obtained. That of Al and Ce elements in long needle-like Al-Ce precipitates is close to 10:3 (Fig. 5(b)), while the atomic ratio of Al, Mn, and Ce elements in short rod-like Al-Mn-Ce precipitates is close to 10:7:2 (Fig. 5(c)). It is of interest that Zn generally appears together with Mg and Al elements, and the magnified observation of the precipitate (Fig. 6(b)) reveals that it has a lamellar internal structure. The corresponding EDS mapping results in Fig. 6(d,e) reflect that the Al and Zn elements in the precipitate are alternately distributed, and the atomic ratio of Mg, Al, and Zn elements is about 6:4:1 (Fig. 5(a) and Fig. 6(f)), demonstrating the typical eutectic structure[47]. Combined with the XRD results in Fig. 7, it is indicated that the precipitates at grain boundaries with lamellar internal structure are the ternary eutectic of $MgZn_2$, $Mg_{17}Al_{12}$, and α-Mg[48], and the detailed formation mechanism was elaborated in our previous work[49].

It is noteworthy that O element is also detected in the precipitates at grain boundaries. The results are shown in the EDS pattern in Fig. 6(f). These O elements originate from the residual magnesium oxides during the smelting process[50-52]. Kondoh Kalso et al.[51] and M Russell-Stevens et al.[52] also reported the coexistence of $Mg_{17}Al_{12}$ and MgO at grain boundaries. Since the oxidation of the melt during the smelting process is difficult to avoid completely, although they were protected by the shielding gas. Hence, the residual insoluble oxides after slagging-off are then expelled to the crystallization frontiers and solidify at the grain boundaries. Meanwhile, the $Mg_{17}Al_{12}$ and $MgZn_2$ are also precipitated at the grain boundaries due to their eutectic point being lower than the melting point of α-Mg[49]. However, the distribution of these precipitates at grain boundaries has a typical splitting effect on the matrix due to the huge difference in elastic

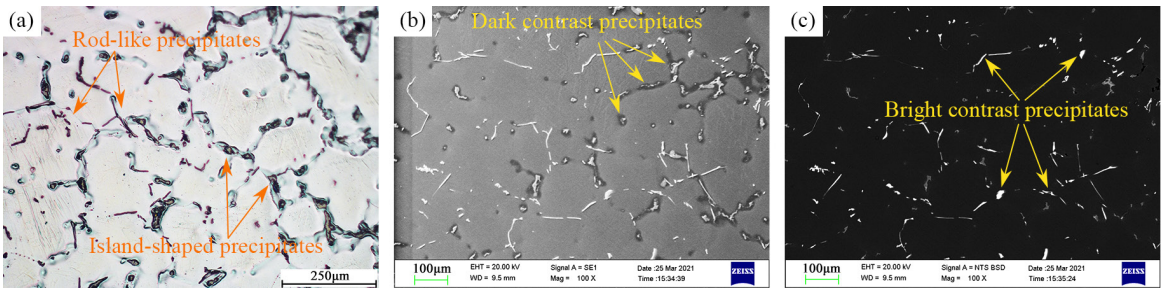

Figure 3. The microstructure of the base metal. (a) OM image, (b) SEM image, (c) BSE image.

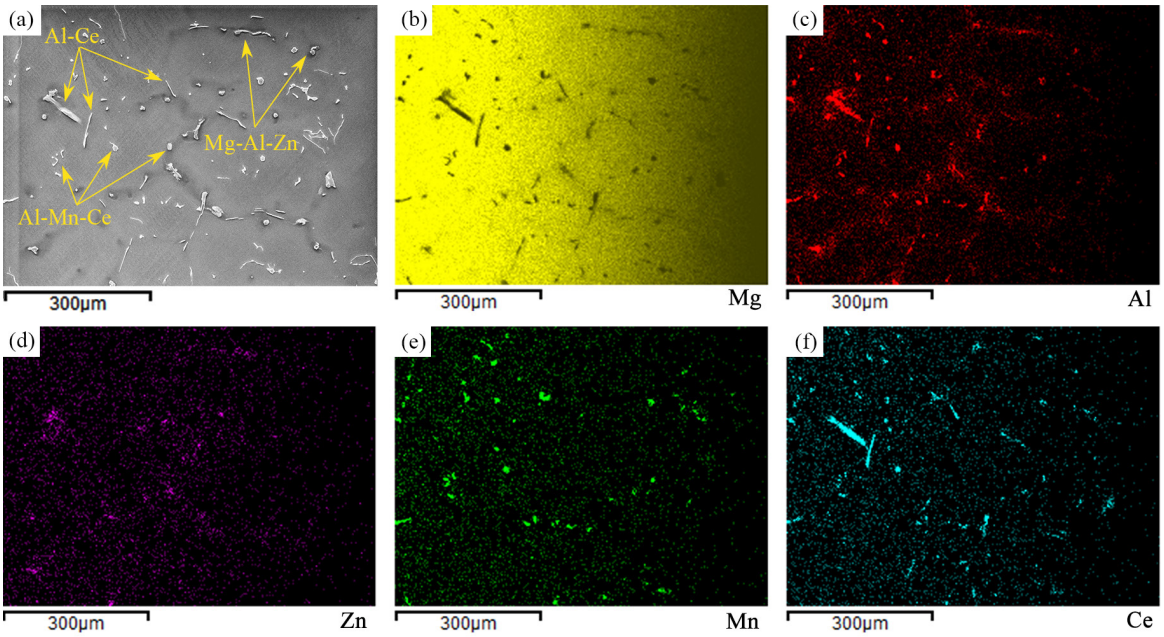

Figure 4. The EDS mapping results of the base metal. (a) EDS mapping position, (b-f) the distribution of Mg, Al, Zn, Mn, and Ce elements.

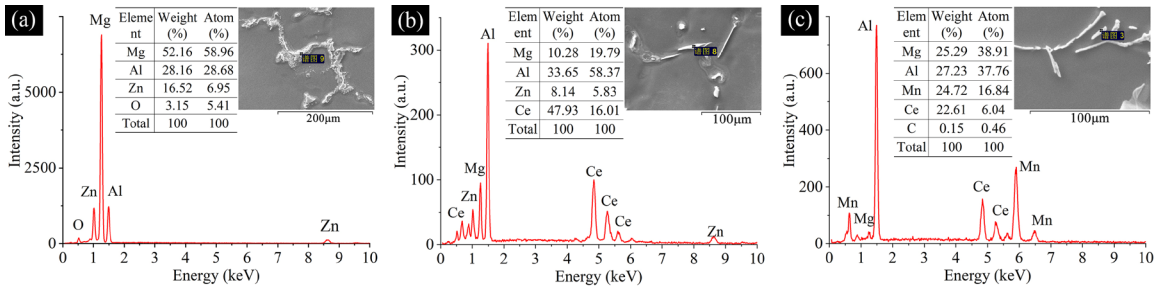

Figure 5. EDS results of the precipitates in base metal. (a) $Mg_{17}Al_{12}$, (b) $Al_{11}Ce_3$, (c) $Al_{10}Ce_2Mn_7$.

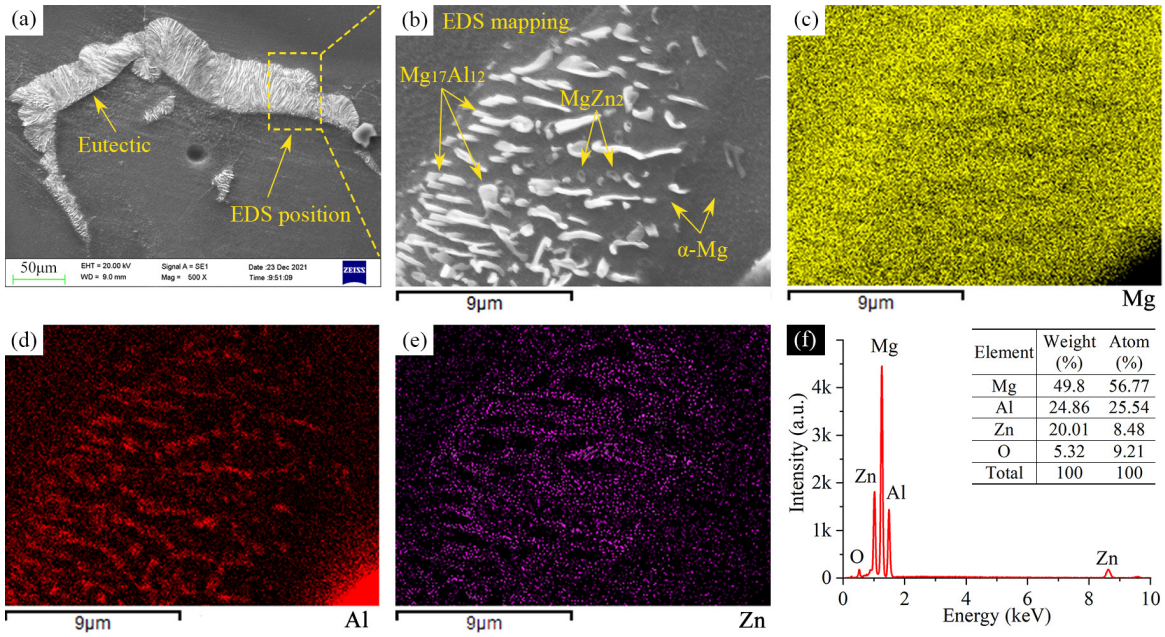

Figure 6. The ternary eutectic of α-Mg, $Mg_{17}Al_{12}$, and $MgZn_2$. (a) the eutectic at grain boundaries, (b) magnified view of the eutectic, (c-e) the distribution of Mg, Al, and Zn elements, (f) the spectrum of EDS mapping.

constants between α-Mg and intermetallics or precipitates such as $Mg_{17}Al_{12}$, $MgZn_2$, and MgO[50], which easily becomes the crack sources. The resulting cracks were photographed in our previous work[49].

X-ray diffraction was employed to further verify the phase composition of the base metal. The results are shown in Fig. 7. Combined with the EDS results in Fig. 4-6, it is clear that the major precipitates in the alloy, such as Al-Mn-Ce, Al-Ce, Mg-Al, and Mg-Zn precipitates, are essentially the $Al_{10}Ce_2Mn_7$, $Al_{11}Ce_3$, $Mg_{17}Al_{12}$, and $MgZn_2$, respectively. At this point, the microstructure and phase composition of the base metal are clearly characterized.

In fact, welding is a process of thermal cycle; hence the thermodynamic stability of the precipitates in base metal determines the post-weld microstructure and mechanical properties of the joint directly, including fusion zone (FZ) and heat-affected zone (HAZ)[53]. In order to elucidate the microstructure evolution and softening mechanism of the HAZ during thermal cycling, a solid solution treatment was carried out for the base metal, and the microstructure of the solution treated base metal is shown in Fig. 8. Apparently, most of the precipitates at grain boundaries formed by conventional alloying elements (Al, Mg, Zn, etc.) are almost completely dissolved after solution treatment, as shown in Fig. 8(a,b), indicating the poor thermal stability of these conventional precipitates. However, the dissolution of the precipitates directly leads to a reduction of the obstacles that pin dislocations and hinder dislocation motion. As a result, the slip resistance of grain boundaries is reduced, and the tensile strength of the alloy decreases accordingly, which is the mechanism of the so-called softening[54]. It is noteworthy that the short rod-like $Al_{10}Ce_2Mn_7$ and the long needle-like $Al_{11}Ce_3$ were not dissolved after solution treatment but still remained in the grains or at the grain boundaries, as verified through the EDS mapping results in Fig. 8(c-f). It is clear that the undissolved rare-earth precipitates partly maintain the original precipitated-phase strengthening effect of the alloy[55], which may be beneficial for reducing the softening of the HAZ after the thermal cycle. Hence, more experiments are needed for further exploring the detailed influence mechanism of rare-earth precipitates on the FZ and HAZ.

3.2. Microstructure and composition of the welded joint

The rare-earth magnesium alloy sheets were laser welded, and the cross-sectional morphology of the obtained joint is shown in Fig. 9. Clearly, the magnesium alloy sheets are effectively connected under the current welding process without obvious welding defects and collapse. The fusion zone is funnel-shaped, and the center of the upper surface of the weld is slightly raised. The depth of the molten pool is 1488μm, the width of the upper surface of the fusion zone is 997μm, and the width of the fusion zone on the contact interface of the magnesium alloy sheets is 842μm. It is of interest that a typical heat-affected zone is not observed near the bonded interface of the fusion zone and base metal.

A magnified observation of the bonded interface of the fusion zone and base metal reveals a significant difference in microstructure on both sides of the interface (Fig. 10(a,b)). That is, the structures in fusion zone are all transformed into dendrites (Fig. 10(c)). In contrast, the grains in base metal and heat-affected zone remained equiaxed. A small amount of granular and short rod-like precipitates are randomly distributed in the fusion zone, in which the diameter of the particles is about 15μm, and the size of the short rod-like precipitates is about 5×20 μm, as shown in Fig. 10(d,e). It is of interest that the particles in fusion zone are similar in size to those in base metal, but the length of the short rod-like precipitates is significantly shorter than that of the long needle-like or rod-like precipitates in base metal. The comparison is clearly displayed in Fig. 10(d,e). In addition, obvious boundaries of HAZ are not observed outside the fusion area, but a small quantity of coral-like precipitates are found distributing at the grain boundaries on the base metal side, which is within a distance of 100-200 μm from the edge of fusion zone, as shown in Fig. 10(d,e). By comparing the microstructure of base metal in Fig. 3, Fig. 4, and Fig. 10(f), it is clear that the coral-like precipitates are the heat-affected products of welding thermal cycle.

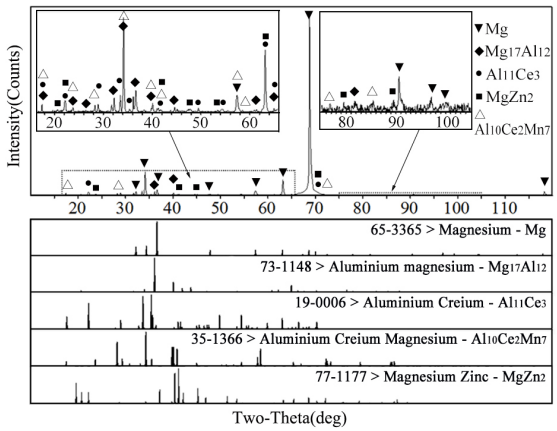

Figure 7. The phase composition of the base metal.

As a matter of fact, the solution experiment of base metal has revealed that the $Mg_{17}Al_{12}$ and $MgZn_2$ at grain boundaries are unstable during thermal cycling, which is a good explanation for the microstructure evolution of the HAZ. The research results of Ragani et al.[5] and Luo[7] indicated that $Mg_{17}Al_{12}$ softened when the temperature was above 120°C[4,5], and the melting point of $Mg_{17}Al_{12}$ was only 473°C[6,7]; whereas $MgZn_2$ had a melting point of 808°C[9], but its eutectic point in magnesium matrix was 416°C[56]. As a comparison, the melting points of $Al_{10}Ce_2Mn_7$ and typical $Al_{11}Ce_3$ are as high as 1150°C[57,58] and 1235°C[6], respectively. During the thermal cycling of low-power laser welding, the temperature in HAZ is not that high, which is apparently lower than the melting

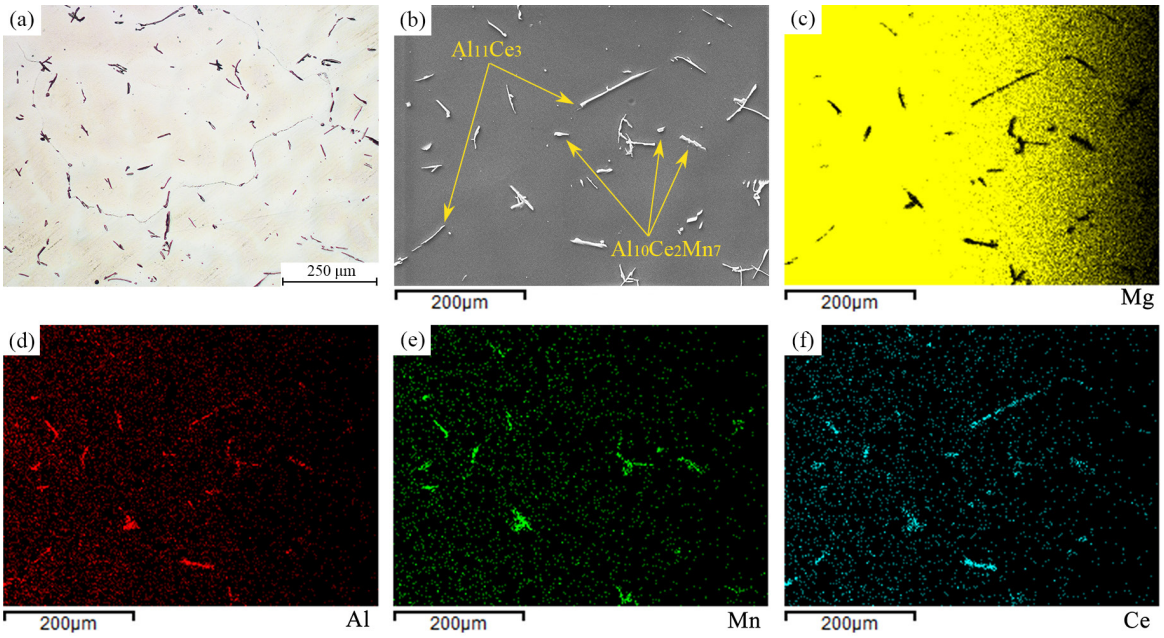

Figure 8. The microstructure of the solution-treated base metal. (a) OM image of solution treated BM, (b) EDS mapping position, (c-f) the distribution of Mg, Al, Zn, Mn, and Ce elements.

point of magnesium alloy (650°C)[59], but higher than the melting temperature of $Mg_{17}Al_{12}$ (437°C). Consequently, the island-shaped $Mg_{17}Al_{12}$ in HAZ melts instantaneously during the brief welding thermal cycle. Then flows and aggregates at the grain boundaries together with the lamellar semi-molten $MgZn_2$, forming the resulting larger-sized, spherical or round-headed island-shaped precipitates with a coral-like internal structure under the combined effect of liquid surface tension and limitation of narrow spaces at grain boundaries[60]. The typical precipitates in HAZ are shown in Fig. 10(d,e). It is worth noting that the welding thermal cycle has little effect on $Al_{10}Ce_2Mn_7$ and $Al_{11}Ce_3$ precipitates in HAZ. Therefore, the morphology and structure of grains in HAZ remain almost the same as that of base metal, and the width of the HAZ in rare-earth magnesium alloy laser welded joint is relatively narrow.

SEM and EDS were employed to further analyze the microstructure and elemental composition of FZ. The magnified observation in Fig. 11(a,b,c) suggests that the grains in FZ have a typical dendritic structure. The width of the dendrite arms is 2-5 μm (Fig. 11(c)). A large number of tiny particles are precipitated along the edge of dendrites, all of which are less than 1μm in size. Moreover, the SEM image in Fig. 11(d) finds several large-sized rod-like and needle-shaped precipitates, which are significantly different in morphology from the tiny particles and α-Mg matrix. The sizes of the precipitates are 3×8 μm and 1×8 μm, respectively. EDS results in Fig. 11(e,f) reveal that the atomic ratio of Al, Mn, Ce elements in the short rod-like precipitate is about 5:3:1; while that of Al and Ce in the needle-like precipitate is close to 3:1. It is clear that the precipitates are $Al_{10}Ce_2Mn_7$ and $Al_{11}Ce_3$ respectively, combined with the XRD results in Fig. 7. The above findings indicate that rare-earth precipitates can still be precipitated in fusion zone at elevated welding temperatures.

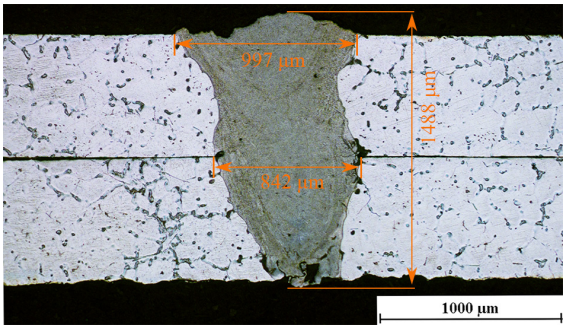

Figure 9. The cross-sectional morphology of the welded joint.

At the bonded interface of FZ and base metal, fusion zone side, the number of tiny particles rises dramatically, forming aggregates with sizes of about 2×8 μm at the crystallization frontier, as shown in Fig. 12(a,b). While on the heat-affected zone side, spherical and round-headed island-shaped precipitates with coral-like internal structures appear at grain boundaries (Fig. 12(c)). EDS dotting results in Fig. 12(e) and Fig. 12(f) reflect that the elemental composition of the above two precipitates is basically the same, which are both composed of Mg, Al, and Zn elements with similar atomic ratios of about 12:4:1. Combined with the composition of base metal and the binary phase diagrams of Mg-Al and Mg-Zn[56,61], it is inferred that those precipitates are the eutectic of $Mg_{17}Al_{12}$ and $MgZn_2$[62]. Moreover, the BSE image in Fig. 12(d) further verifies that the coral-like precipitates are made up of several lamellar substances with obvious contrast differences, which are the typical morphology of eutectic.

Obviously, the composition and precipitation mechanism of these two precipitates are similar. The main difference is that the fusion zone is remelted. Hence, the $Mg_{17}Al_{12}$ and $MgZn_2$ in FZ are precipitated through eutectic reactions, thus forming tiny particles with a size of only about 500 nm at the edge of dendrites under the high cooling rate of laser welding. In contrast, the HAZ is not melted, but the

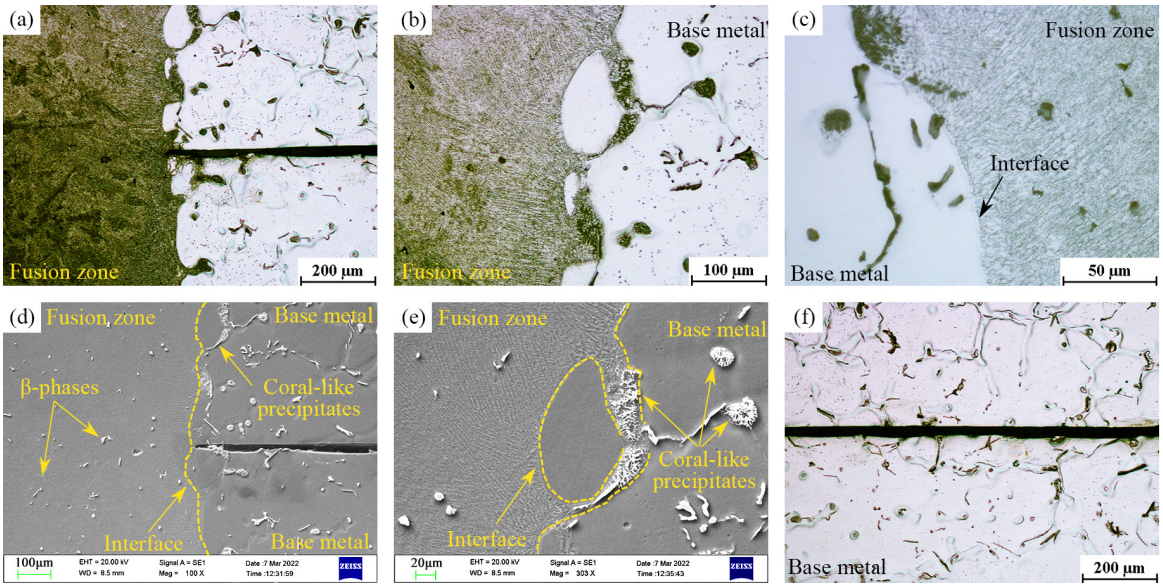

Figure 10. Microstructure of the welded joint. (a) contact interface of the sheets, (b) bonded interface of BM and FZ, (c) magnified view of the bonded interface, (d) SEM image of the joint, (e) precipitates near the interface, (f) OM image of BM.

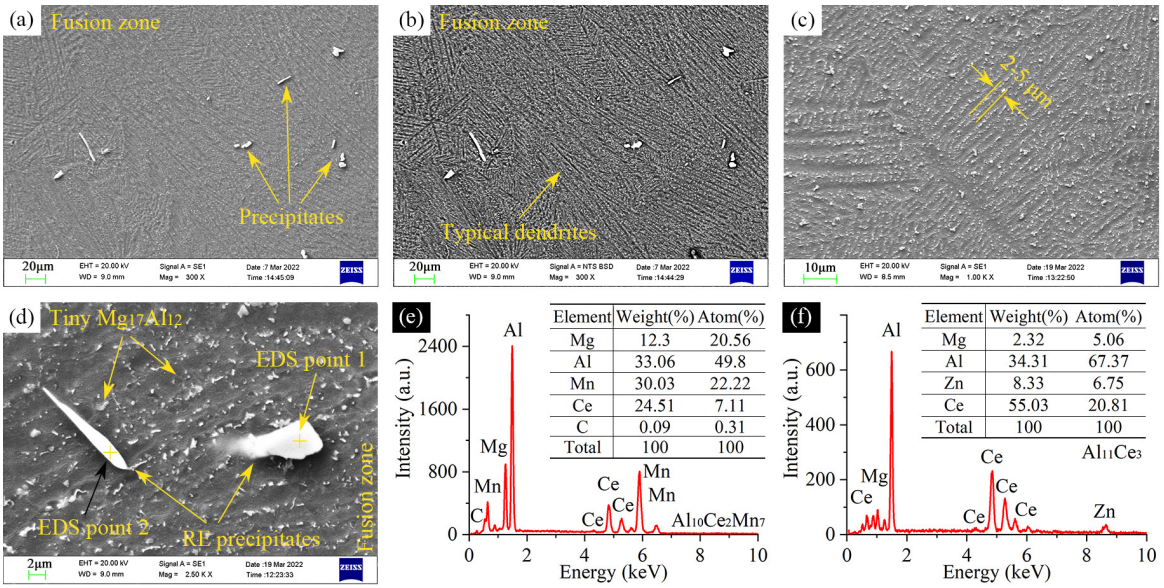

Figure 11. The SEM and EDS results of the fusion zone. (a) SEM image of FZ, (b) BSE image of FZ, (c) dendrites in FZ, (d) large-sized RE precipitates in FZ, (e) EDS spectrum of point 1-$Al_{10}Ce_2Mn_7$, (f) EDS spectrum of point 2-$Al_{11}Ce_3$.

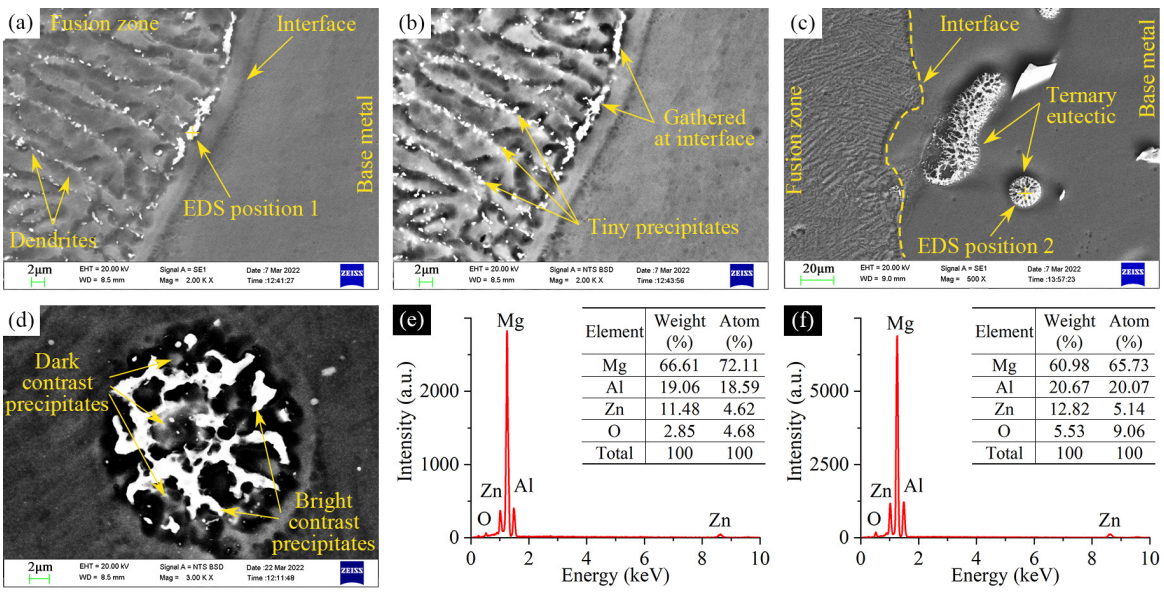

Figure 12. The SEM and EDS results of the HAZ. (a) precipitates near the bonded interface, (b)BSE image of the precipitates, (c) precipitates in the HAZ, (d) BSE image of the coral-like precipitates, (e) EDS spectrum of position 1, (f) EDS spectrum of position 2.

temperature in HAZ is higher than the melting point of $Mg_{17}Al_{12}$ during the brief welding thermal cycle. Consequently, the original island-shaped $Mg_{17}Al_{12}$ and $MgZn_2$ eutectics at grain boundaries melt and flow together, forming larger-sized and rounded-shaped precipitates instead under the combined effect of liquid surface tension and confinement of narrow grain boundary spaces[60]. However, due to the significant difference between the elastic constants of these precipitates and base metal, the large-sized, brittle and hard precipitates at grain boundaries have a typical splitting effect on the alloy during plastic deformation and easily become the cracking sources[11]. This is one of the main reasons why HAZ is extremely susceptible to softening and fracture, and highly thermally stable precipitates are urgently needed for reducing the softening of the HAZ.

3.3. Strengthening mechanism of rare-earth precipitates on welded joint

Microhardness test was used to evaluate the influence of the welding thermal cycle on the fusion zone and heat-affected zone, and the results are shown in Fig. 13. Apparently, the overall microhardness of the FZ is dramatically improved and

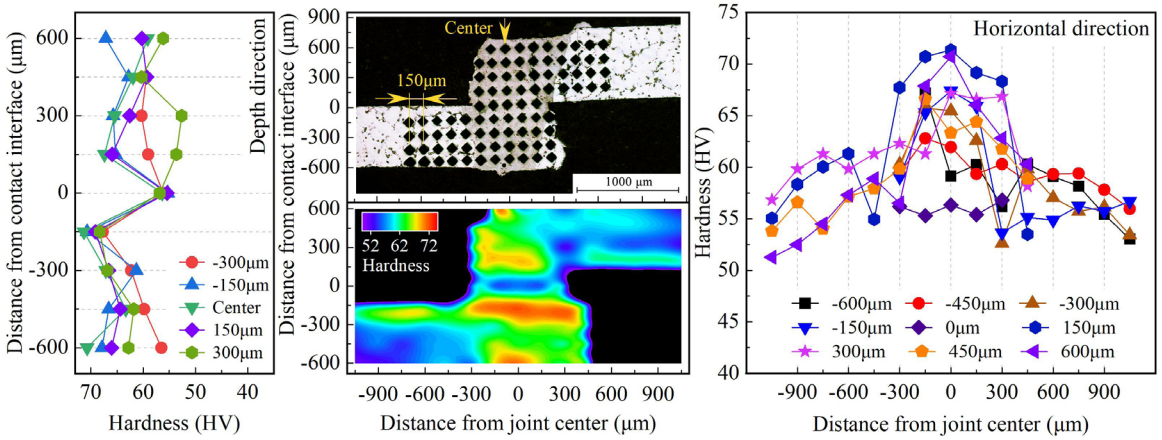

Figure 13. The micro-hardness distribution of the welded joint.

is significantly higher than that of the base metal. According to the hardness curves in the vertical direction of the fusion zone, it is found that the hardness values in the upper sheet are relatively stable. However, as the test depth increases, the hardness increases slightly accordingly. For instance, at 150μm above the contact interface of the two sheets, the average hardness reaches 62.26HV. However, the lowest hardness value occurs at the contact interface, where the average hardness is only 56.00HV, but it is still higher than that of the base metal (54.18HV). It is noteworthy that the hardness measured at the bottom sheet where near the contact interface is significantly higher than that of the upper sheet, and the closer the contact interface, the higher the hardness. Among these, the average hardness measured at the bottom sheet, which is 150μm below the contact interface, is 69.46HV, which is 28.2% higher than that of the base metal. While the hardness measured at the other region of the bottom sheet is basically the same as that of the upper sheet, and the variation of these values is relatively small.

In addition, the hardness curves in the horizontal direction find that the hardness in the center of the fusion zone is the highest. However, as the distance from the center increases, the hardness values on both sides gradually decrease, and the values are basically symmetrical. Interestingly, in the vicinity of the bonded interface of FZ and BM, where is about 300μm away from the center of FZ, obvious inflection points are observed in the hardness curves. For example, the hardness drops to 53.68HV and 54.94HV at positions near the right and left edges of the fusion zone, which were 150μm above the contact interface of sheets. The results show that the hardness of this region is lower than that of the base metal, demonstrating the softening of the HAZ due to the welding thermal cycle. The test results and indentations are shown in Fig. 13.

In order to further illustrate the softening mechanism of the HAZ and the strengthening effect of tiny particles on the FZ, a specially designed solution treatment was carried out for the welded joint, and the microhardness test was performed along the bonded interface of FZ and BM, as well as the right and left sides of the bonded interface. The hardness results of the joint with and without solution treatment are illustrated in Fig. 14(a-c) and Table 2, and the indentations are displayed in Fig. 14(d).

As can be seen in Fig. 14(a) and Table 2, the average hardness of the HAZ in the untreated joint is 49.23HV. It is much lower than the 54.18HV of the base metal (Fig. 14(c)), indicating the softening of the HAZ, and the softening amplitude is 9.14%. However, it is of interest that this value is close to that of the solution-treated base metal (48.46HV). The comparison further finds that the value is significantly higher than the hardness of the rare-earth free magnesium alloy (the types and contents of other alloying elements in the alloy are the same) after solution treatment (41.46HV). The findings above suggest that the impact of welding thermal cycle on the hardness of HAZ is similar to that of the solution treatment, which can be easily verified through the microstructure analysis. And apparently, both conventional and rare-earth precipitates improve the hardness of the alloy. Whereas rare-earth precipitates in base metal and HAZ are undissolved during solution treatment or thermal cycling, resulting in the main precipitates in HAZ remain basically unchanged, which is crucial for reducing the softening of the HAZ during thermal cycling.

Besides, the average hardness measured at the untreated fusion zone, which is 150μm from the bonded interface, is 56.47HV. The comparison shows that the value is higher than that of the base metal (54.18HV), indicating that the small-sized, uniformly distributed particles are beneficial for further improving the hardness of the joint. However, due to the poor thermodynamic stability of $Mg_{17}Al_{12}$ and $MgZn_2$, a reduction of 5.15% in hardness is observed at the same position of the FZ after solution treatment. The value is decreased to 53.56HV, which is slightly lower than that of the untreated base metal (54.18HV), demonstrating that the tiny precipitates in the fusion zone may be composed of both rare-earth precipitates and conventional precipitates. The residual rare-earth precipitates in FZ after solution treatment guarantee FZ good mechanical properties, even though the conventional precipitates are dissolved.

4. Discussion

In fact, the strengthening and softening mechanism of welded joints can be well explained by analyzing the influence of thermal cycling on the microstructure of magnesium

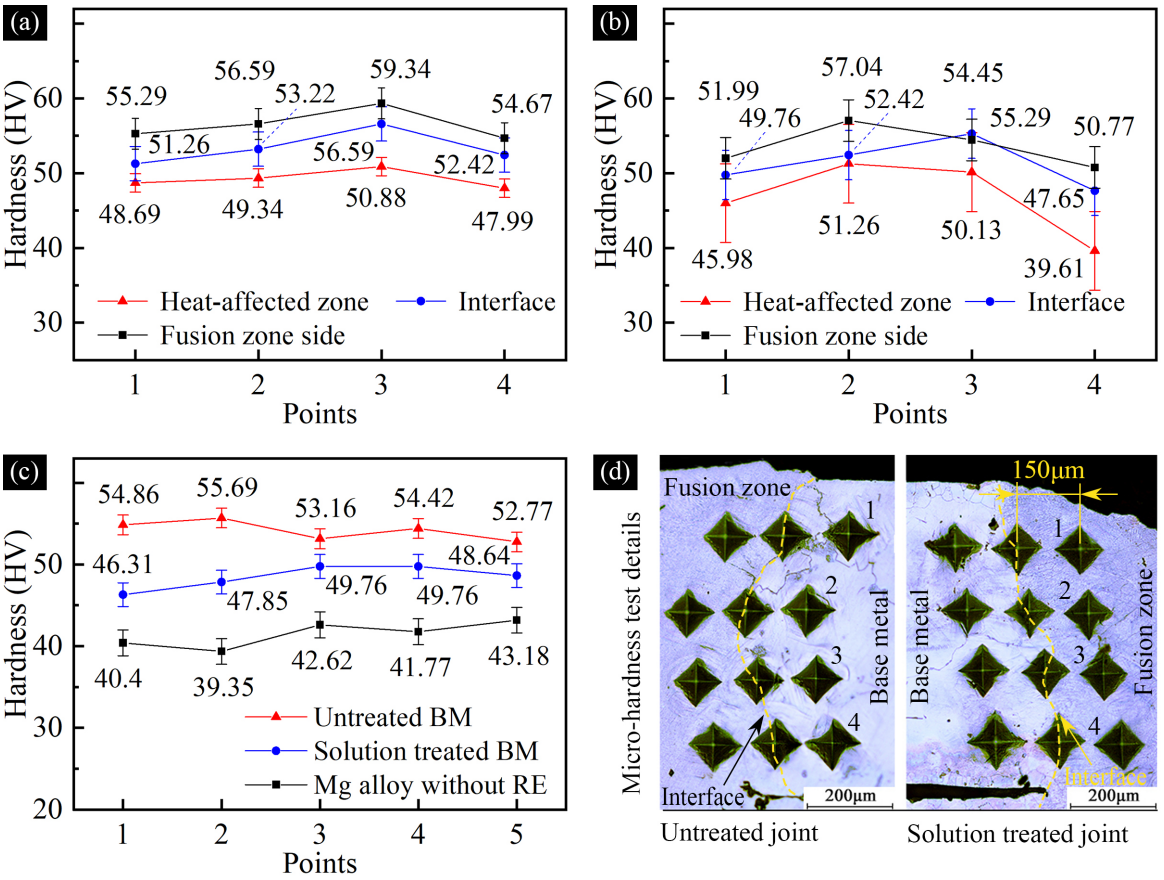

Figure 14. Specially designed micro-hardness test for samples with and without solution treatment. (a) welded joint, (b) solution treated welded joint, (c) hardness of BM and rare-earth free magnesium alloy, (d) indentations of the welded joints with and without solution treatment.

Table 2. The hardness of the joints with and without solution treatment.

Hardness (HV)	Untreated joint			Solution treated joint			Untreated base metal	Solution treated base metal	Solution treated magnesium alloy without RE element
	HAZ	Bonded interface	FZ	HAZ	Bonded interface	FZ			
1	48.69	51.26	55.29	45.98	49.76	51.99	54.86	46.31	40.4
2	49.34	53.22	56.59	51.26	52.42	57.04	55.69	47.85	39.35
3	50.88	56.59	59.34	50.13	55.29	54.45	53.16	49.76	42.62
4	47.99	52.42	54.67	39.61	47.65	50.77	54.42	49.76	41.77
5	-	-	-	-	-	-	52.77	48.64	43.18
Average	49.23	53.37	56.47	46.75	51.28	53.56	54.18	48.46	41.46
Standard deviation	1.23	2.29	2.07	5.27	3.31	2.78	1.21	1.45	1.58

alloys. The in-situ observation of the precipitates in the fusion zone before and after solution treatment is shown in Fig. 15(a-d). It is evident that the uniformly distributed, micron-sized precipitates at the edge of dendrites are the key to the substantial improvement of the hardness of the FZ. These tiny particles increase the dislocation density, pinning dislocations and hindering the slip of the grain boundaries, thus strengthening the FZ effectively. Meanwhile, the BSE and EDS images find that the tiny particles in FZ have obvious contrast differences. EDS results conclude that the bright contrast particles are composed of Al, Ce elements or Al, Mn, Ce elements (Fig. 15(e,f)), while the dark contrast precipitates are composed of Mg, Al, and Zn elements. Combined with the atomic ratio obtained by EDS and the composition discussion in section 3.2, it is evident that the tiny particles at the edge of dendrites are composed of both

conventional precipitates (such as $Mg_{17}Al_{12}$, $MgZn_2$) and rare-earth precipitates (such as $Al_{11}Ce_3$ and $Al_{10}Ce_2Mn_7$).

However, during the solution treatment at 440°C, most of the $Mg_{17}Al_{12}$ at the edge of the dendrites dissolved into the matrix (Fig. 15(c,d)), resulting in a decrease in both dislocation density and slip resistance of the grain boundaries, which is the so-called softening[63]. But residual particles can still be found at the edge of the dendrites after solution treatment. EDS results in Fig. 15(e,f) confirm that the residual particles are mainly rare-earth precipitates with good thermodynamic stability, which continue resisting the slip of the grain boundaries. As a result, although the hardness of the FZ after the solid solution decreases, it still maintains at a relatively high level.

The improvement of mechanical properties of magnesium alloys by rare-earth precipitates can also be verified by observing the hindrance of dislocation motion by the precipitates. Fig. 16(a) shows the cross-sectional morphology of a tensile fracture of the base metal (0.4wt.% Ce added), where the obstruction of dislocation motion by $Al_{11}Ce_3$ is clearly displayed. Typical parallel slip lines (Fig. 16(b,c)) indicate the initiation of the dislocations[64,65]. However, due to the huge difference in elastic constants between $Al_{11}Ce_3$ and α-Mg, the hard and brittle $Al_{11}Ce_3$ cannot respond to the deformation of the matrix but hinders the dislocation motion in the matrix instead, and eventually breaks into pieces under the deformation resistance. This is a good explanation for the reason why rare-earth precipitates improve the hardness of welded joints.

In summary, the strengthening effect of rare-earth precipitates is not limited to the fusion zone, its strengthening mechanism for HAZ is also consistent. That is, on the one hand, a reinforced structure is formed in the alloy in which the rare-earth precipitates are mixed with the conventional precipitates. That functions especially for the fusion zone, where the micron-sized rare-earth particles and conventional particles ($Mg_{17}Al_{12}$ and $MgZn_2$) are precipitated almost simultaneously and mixed together under the high cooling rate of laser welding, which both increases the dislocation density and pins the dislocations effectively, thus strengthening the joint. On the other hand, the thermodynamically stable rare-earth precipitates rarely dissolve or decompose during welding thermal cycling. Therefore, the

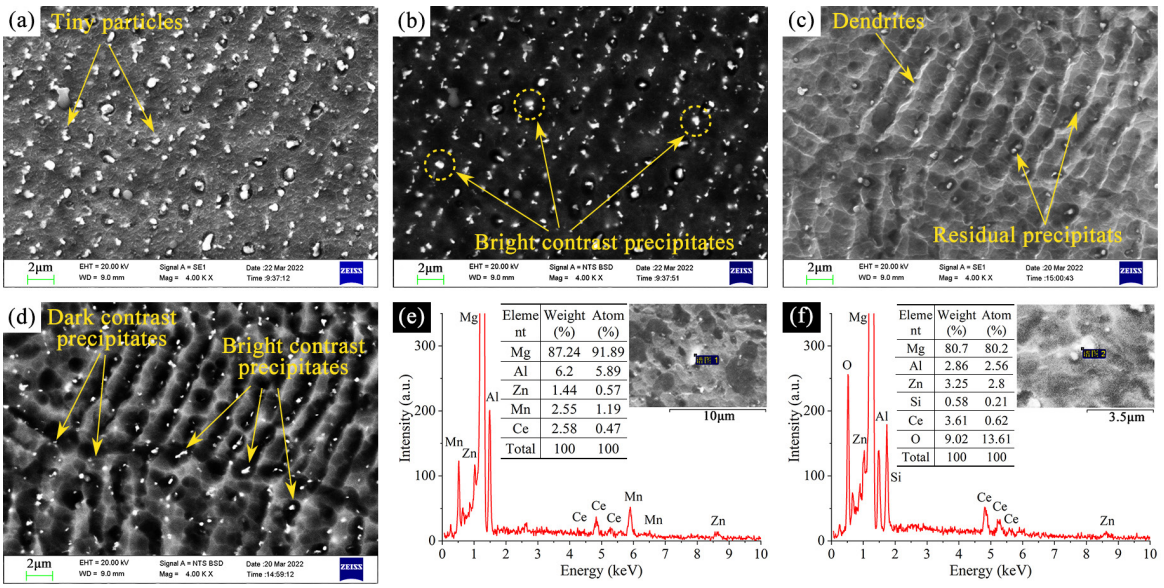

Figure 15. Solution experiments of the tiny particles in fusion zone. (a) microstructure of the FZ, (b) BSE image of the FZ, (c) in-suit morphology of the FZ after solution treatment, (d) BSE image of the FZ after solution treatment, (e) tiny $Al_{10}Ce_2Mn_7$ in FZ, (f) tiny $Al_{11}Ce_3$ in FZ.

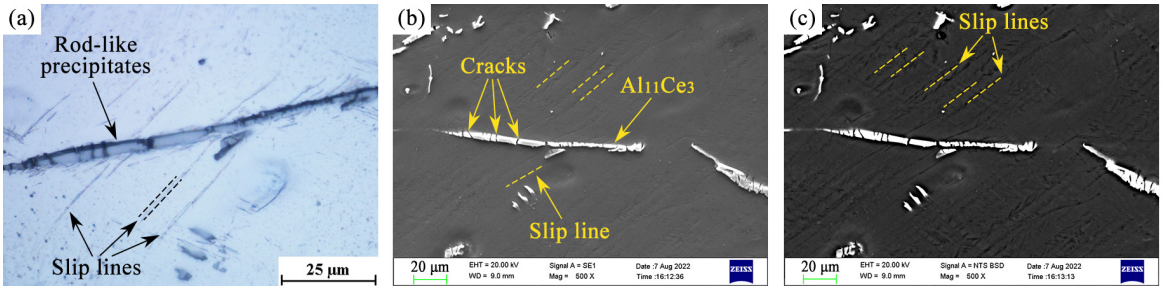

Figure 16. Obstruction of the dislocations by precipitates. (a) OM image of the broken precipitates and slip lines, (b) SEM image of the broken precipitates, (c) BSE image of the broken precipitates.

rare-earth precipitates in both HAZ and FZ remain basically unchanged after the thermal cycle, which partly improves the stability of the microstructure in HAZ and FZ, although the conventional precipitates are dissolved.

5. Conclusion

(1) The microstructure and composition analysis found that the base metal was composed of equiaxed crystals with a size of 300-400 μm. The main precipitates in the alloy were the eutectic of $Mg_{17}Al_{12}$ and $MgZn_2$ at grain boundaries, and granular $Al_{10}Ce_2Mn_7$ and long needle-like $Al_{11}Ce_3$ in grains.

(2) The microstructure analysis of the FZ revealed that the grains in FZ were transformed completely into dendrites, and the width of the dendrite arms was 2-5 μm. Large numbers of tiny particles with a size of less than 1μm were precipitated at the edge of the dendrites. Component analysis indicated that these particles were the randomly distributed $Mg_{17}Al_{12}$, $MgZn_2$, $Al_{11}Ce_3$, and $Al_{10}Ce_2Mn_7$ precipitates.

(3) The HAZ of laser-welded joints was relatively small, with a width of only 100-200 μm. The welding thermal cycle had little influence on the morphology and composition of rare-earth precipitates in HAZ, but it had a great impact on the conventional precipitates (such as $Mg_{17}Al_{12}$ and $MgZn_2$). Wherein the $Mg_{17}Al_{12}$ and $MgZn_2$ in HAZ melted and re-formed larger-sized precipitates with coral-like internal structures at grain boundaries, resulting in the softening of the HAZ.

(4) The microhardness test results reflected that the micron-sized, uniformly distributed particles at the edge of dendrites played a crucial role in improving the hardness of the FZ. The reinforced structure consisted of rare-earth precipitates and conventional precipitates was beneficial for improving the mechanical properties of both FZ and HAZ.

(5) The solution experiments of the welded joints found that the rare-earth precipitates were thermodynamically stable. They maintained the hardness of the FZ after solution treatment at a level close to that of the base metal, even though the conventional precipitates were dissolved, demonstrating that the rare-earth precipitates were beneficial for improving the thermodynamic stability of the welded joint, which is crucial for welds serving in thermal cycling conditions.

6. Acknowledgments

The work in this paper was supported by (1) Key Research and Development Program of Jiangxi Province (No.20203BBG73070); (2) Natural Science Foundation of Jiangxi Province-General Project (No.20202BABA204009); (3) Jiangxi Provincial Technology Innovation Guidance Program (Science and Technology Cooperation Special Project) (20212BDH81014)

7. References

1. Lloyd JT, Jannotti PA, Jones TL. An overview of penetration behavior in magnesium alloys. Mech Mater. 2021;162:104038.
2. Nie KB, Wang XJ, Deng KK, Hu XS, Wu K. Magnesium matrix composite reinforced by nanoparticles–a review. Journal of Magnesium and Alloys. 2021;9(1):57-77.
3. Wahba M, Mizutani M, Kawahito Y, Katayama S. Laser welding of die-cast AZ91D magnesium alloy. Mater Des. 2012;33:569-76.
4. Zhang Q. The micro-structure and high temperature properties of heat-resistant magnesium alloys [dissertation]. Sichuan: Sichuan University; 2007.
5. Ragani J, Donnadieu P, Tassin C, Blandin JJ. High-temperature deformation of the γ-Mg17Al12 complex metallic alloy. Scr Mater. 2011;65(3):253-6.
6. Zhang S. Effects of Al-Mn master alloys addition on the micro structures and mechanical properties at high temperture of Mg-Al-Mn systerm alloys [dissertation]. Wuhan: Wuhan University of Science and Technology; 2016.
7. Luo AA. Recent magnesium alloy development for elevated temperature applications. Int Mater Rev. 2004;49(1):13-30.
8. Morishita M, Koyama K, Shikada S, Kusumoto M. Calorimetric study of Mg2Zn3. Int J Mater Res. 2005;96(1):32-7.
9. Mao PL, Yu B, Liu Z, Wang F, YangJu Y. Mechanical properties and electronic structures of MgCu2, Mg2Ca and MgZn2 Laves phases by first principles calculations. Trans Nonferrous Met Soc China. 2014;24(9):2920-9.
10. Windmann M, Röttger A, Kügler H, Theisen W. Microstructure and mechanical properties of the heat-affected zone in laser-welded/brazed steel 22MnB5–AA6016 aluminum/AZ31 magnesium alloy. J Mater Process Technol. 2017;247:11-8.
11. Wang L, Huang J, Peng Y, Wu Y. Precipitates evolution in the heat affected zone of Mg-Gd-Y-Zr alloy in T6 condition during laser welding. Mater Charact. 2019;154:386-94.
12. Lin CM, Tsai HL, Lee CL, Chou DS, Huang JC. Evolution of microstructures and properties of magnesium alloy weldments produced with CO2 laser process. Mater Sci Eng A. 2012;548:12-8.
13. Beiranvand ZM, Ghaini FM, Moosavy HN, Sheikhi M, Torkamany MJ, Moradi M. The relation between magnesium evaporation and laser absorption and weld penetration in pulsed laser welding of aluminum alloys: experimental and numerical investigations. Opt Laser Technol. 2020;128:106170.
14. Cao X, Jahazi M, Immarigeon JP, Wallace W. A review of laser welding techniques for magnesium alloys. J Mater Process Technol. 2006;171(2):188-204.
15. Czerwinski F. Magnesium alloys: design, processing and properties. Reijeka: InTech; 2011. Welding and joining of magnesium alloys; p. 469-490.
16. Luo Q, Guo Y, Liu B, Feng Y, Zhang J, Li Q et al. Thermodynamics and kinetics of phase transformation in rare earth–magnesium alloys: A critical review. J Mater Sci Technol. 2020;44:171-90.
17. Kondori B, Mahmudi R. Effect of Ca additions on the microstructure, thermal stability and mechanical properties of a cast AM60 magnesium alloy. Mater Sci Eng A. 2010;527(7-8):2014-21.
18. Hirai K, Somekawa H, Takigawa Y, Higashi K. Effects of Ca and Sr addition on mechanical properties of a cast AZ91 magnesium alloy at room and elevated temperature. Mater Sci Eng A. 2005;403(1-2):276-80.
19. Wang M, Xiao DH, Liu WS. Effect of Si addition on microstructure and properties of magnesium alloys with high Al and Zn contents. Vacuum. 2017;141:144-51.
20. Marjani O, Emamy M, Mirzadeh H. Mechanical behavior of as-cast and extruded Mg-Si-Ni-Ca magnesium alloys. J Mater Eng Perform. 2020;29(11):7728-35.
21. Bai J, Sun Y, Xun S, Xue F, Zhu T. Microstructure and tensile creep behavior of Mg–4Al based magnesium alloys with alkaline-earth elements Sr and Ca additions. Mater Sci Eng A. 2006;419(1-2):181-8.

22. Afsharnaderi A, Lotfpour M, Mirzadeh H, Emamy M, Malekan M. Enhanced mechanical properties of as-cast AZ91 magnesium alloy by combined RE-Sr addition and hot extrusion. Mater Sci Eng A. 2020;792:139817.
23. Kumar P, Mondal AK, Chowdhury SG, Krishna G, Ray AK. Influence of additions of Sb and/or Sr on microstructure and tensile creep behaviour of squeeze-cast AZ91D Mg alloy. Mater Sci Eng A. 2017;683:37-45.
24. Zhou SH, Napolitano RE. Phase equilibria and thermodynamic limits for partitionless crystallization in the Al–La binary system. Acta Mater. 2006;54(3):831-40.
25. Luo Q, Zhai C, Gu Q, Zhu W, Li Q. Experimental study and thermodynamic evaluation of Mg–La–Zn system. J Alloys Compd. 2020;814:152297.
26. Kang YB, Pelton AD, Chartrand P, Fuerst CD. Critical evaluation and thermodynamic optimization of the Al–Ce, Al–Y, Al–Sc and Mg–Sc binary systems. Calphad. 2008;32(2):413-22.
27. Gorsse S, Hutchinson CR, Chevalier B, Nie JF. A thermodynamic assessment of the Mg–Nd binary system using random solution and associate models for the liquid phase. J Alloys Compd. 2005;392(1-2):253-62.
28. Zhai C, Luo Q, Cai Q, Guan R, Li Q. Thermodynamically analyzing the formation of Mg12Nd and Mg41Nd5 in Mg-Nd system under a static magnetic field. J Alloys Compd. 2019;773:202-9.
29. Hampl M, Blawert C, Campos MRS, Hort N, Peng Q, Kainer KU et al. Thermodynamic assessment and experimental study of Mg–Gd alloys. J Alloys Compd. 2013;581:166-77.
30. Lukyanova EA, Rokhlin LL, Dobatkina TV, Korolkova IG, Tarytina IE. Investigation of the Mg-rich part of the Mg-Dy-Sm phase diagram. J Phase Equilibria Diffus. 2016;37(6):664-71.
31. Fabrichnaya OB, Lukas HL, Effenberg G, Aldinger F. Thermodynamic optimization in the Mg–Y system. Intermetallics. 2003;11(11-12):1183-8.
32. Zhang X, Kevorkov D, Pekguleryuz MO. Study on the intermetallic phases in the Mg–Ce system: part II. Diffusion couple investigation. J Alloys Compd. 2010;501(2):366-70.
33. Kang YB, Pelton AD, Chartrand P, Spencer P, Fuerst CD. Critical evaluation and thermodynamic optimization of the binary systems in the Mg-Ce-Mn-Y system. J Phase Equilibria Diffus. 2007;28(4):342-54.
34. Shi H, Li Q, Zhang J, Luo Q, Chou KC. Re-assessment of the Mg–Zn–Ce system focusing on the phase equilibria in Mg-rich corner. Calphad. 2020;68:101742.
35. Cheng R, Dong H, Liu W, Jiang B, Xiong S, Liu B etal. Effect of Al-and Ce-content on microstructure of Mg-Al magnesium alloys. Chinese J Mater Res. 2017;31(10):737-42.
36. Zhang X, Kevorkov D, Pekguleryuz M. Stoichiometry study on the binary compounds in the Mg-Ce system-Part I. J Alloys Compd. 2009;475(1-2):361-7.
37. Mezbahul-Islam M, Mostafa A, Medraj M. Essential magnesium alloys binary phase diagrams and their thermochemical data. J Mater. 2014;2014:704283.
38. Zhang X, Kevorkov D, Pekguleryuz MO. Study on the binary intermetallic compounds in the Mg–Ce system. Intermetallics. 2009;17(7):496-503.
39. Zhang D, Yang Q, Guan K, Li B, Wang N, Qing P et al. A high-strength low-rare-earth-alloyed magnesium alloy via traditional hot-extrusion. J Alloys Compd. 2019;810:151967.
40. Gao M, Tang HG, Chen XF, Zeng XY. High power fiber laser arc hybrid welding of AZ31B magnesium alloy. Mater Des. 2012;42:46-54.
41. Li T, Song G, Zhang Z, Liu L. Mechanical Properties and Microstructures of Laser–TIG Welded ME21 Rare Earth Mg Alloy. Materials (Basel). 2019;12(13):2188.
42. Dai J, Huang J, Li M, Li Z, Dong J, Wu Y. Effects of heat treatments on laser welded Mg-rare earth alloy NZ30K. Mater Sci Eng A. 2011;529:401-5.
43. Dai J, Huang J, Li Z, Dong J, Wu Y. Effects of heat input on microstructure and mechanical properties of laser-welded Mg-Rare earth alloy. J Mater Eng Perform. 2013;22(1):64-70.
44. Liu L, Liu X, Liu S. Microstructure of laser-TIG hybrid welds of dissimilar Mg alloy and Al alloy with Ce as interlayer. Scr Mater. 2006;55(4):383-6.
45. Dobriyal RP, Dhindaw BK, Muthukumaran S, Mukherjee SK. Microstructure and properties of friction stir butt-welded AE42 magnesium alloy. Mater Sci Eng A. 2008;477(1-2):243-9.
46. Sirong Y, Xianjun C, Huang Z, Yaohui L. Microstructure and mechanical properties of friction stir welding of AZ31B magnesium alloy added with cerium. J Rare Earths. 2010;28(2):316-20.
47. Fan X, Jiang D, Meng Q, Zhang BY, Tao W. Evolution of eutectic structures in Al-Zn-Mg-Cu alloys during heat treatment. Trans Nonferrous Met Soc China. 2006;16(3):577-81.
48. Takata N, Okano T, Aikawa M, Suzuki A, Kobashi M, Hagihara K. Morphology and mechanical properties of the T-Al6Mg11Zn11 phase in the eutectic microstructure of Al–Zn–Mg ternary alloys. Intermetallics. 2020;124:106881.
49. Chen Y, Zhu Z, Zhou J. Study on the strengthening mechanism of rare earth yttrium on magnesium alloys. Mater Sci Eng A. 2022;850:143513.
50. Gali OA, Shafiei M, Hunter JA, Riahi AR. The influence of hot rolling on oxide development within micro-cracks of aluminum–magnesium alloys. Mater Sci Eng A. 2014;618:129-41.
51. Kondoh K, Fukuda H, Umeda J, Imai H, Fugetsu B, Endo M. Microstructural and mechanical analysis of carbon nanotube reinforced magnesium alloy powder composites. Mater Sci Eng A. 2010;527(16-17):4103-8.
52. Russell-Stevens M, Todd R, Papakyriacou M. Microstructural analysis of a carbon fibre reinforced AZ91D magnesium alloy composite. Surf Interface Anal. 2005;37(3):336-42.
53. Wahba M, Mizutani M, Kawahito Y, Katayama S. Laser welding of die-cast AZ91D magnesium alloy. Mater Des. 2012;33:569-76.
54. Wang H, Zhang Y, Chen K. Modeling of temperature distribution in laser welding of lapped martensitic steel M1500 and softening estimation. J Manuf Sci Eng. 2016;138(11):111006.
55. Dai J, Huang J, Wu Y. Research on laser welding of Mg-rare earth alloy Mg-3Nd-0.2 Zn-0.4 Zr. J Mater Eng Perform. 2012;21(2):208-12.
56. Wasiur-Rahman S, Medraj M. Critical assessment and thermodynamic modeling of the binary Mg–Zn, Ca–Zn and ternary Mg–Ca–Zn systems. Intermetallics. 2009;17(10):847-64.
57. Zhang MJ, Yang XH, Liu YB, Cao ZY, Cheng LR, Pei YL. Effect of graphite content on wear property of graphite/Al2O3/Mg-9Al-1Zn-0.8 Ce composites. Trans Nonferrous Met Soc China. 2010;20(2):207-11.
58. Yang Q, Lv SH, Meng FZ, Guan K, Li BS, Zhang XH et al. Detailed structures and formation mechanisms of well-known Al10RE2Mn7 phase in die-cast Mg–4Al–4RE–0.3 Mn alloy. Acta Metall Engl Lett. 2019;32(2):178-86.
59. Mert F, Oezdemir A, Kainer KU, Hort N Influence of Ce addition on microstructure and mechanical properties of high pressure die cast AM50 magnesium alloy. Trans Nonferrous Met Soc China. 2013;23(1):66-72.
60. Zhu T, Chen ZW, Gao W. Dissolution of eutectic β-Mg17Al12 phase in magnesium AZ91 cast alloy at temperatures close to eutectic temperature. J Mater Eng Perform. 2010;19(6):860-7.
61. Liang P, Su HL, Donnadieu P, Harmelin MG, Quivy A, Ochin P et al. Experimental investigation and thermodynamic calculation of the central part of the Mg–Al phase diagram. Int J Mater Res. 1998;89(8):536-40.

62. Huang L, Liu S, Du Y, Zhang C. Thermal conductivity of the Mg–Al–Zn alloys: experimental measurement and CALPHAD modeling. Calphad. 2018;62:99-108.
63. Powidajko E. Weldability of AZ31B magnesium sheet by laser welding processes [dissertation]. Waterloo: University of Waterloo; 2009.
64. Barnett MR, Keshavarz Z, Ma X. A semianalytical Sachs model for the flow stress of a magnesium alloy. Metall Mater Trans, A Phys Metall Mater Sci. 2006;37(7):2283-93.
65. Ando D, Sutou Y, Koike J. Internal microstructure observation of enhanced grain-boundary sliding at room temperature in AZ31 magnesium alloy. Mater Sci Eng A. 2016;666:94-9.